Computer Methods in Applied Mechanics and Engineering 199 (2010) 1976–1991

Contents lists available at ScienceDirect

Computer Methods in Applied Mechanics and Engineering

journal homepage: www.elsevier.com/locate/cma

Optimal aerodynamic design of airfoils in unsteady viscous flows

D.N. Srinath, Sanjay Mittal

Department of Aerospace Engineering, Indian Institute of Technology Kanpur, Kanpur, UP, 208016, India

ARTICLE INFO

Article history:
Received 10 November 2009
Received in revised form 18 February 2010
Accepted 24 February 2010
Available online 3 March 2010

Keywords:
Shape optimization
Adjoint methods
Unsteady flows
Time accurate
Continuous adjoint
Finite element
Airfoil

ABSTRACT

A continuous adjoint formulation is used to determine optimal airfoil shapes in unsteady viscous flows at $Re = 1 \times 10^4$. The Reynolds number is based on the free-stream speed and the chord length of the airfoil. A finite element method based on streamline-upwind Petrov/Galerkin (SUPG) and pressure-stabilized Petrov/Galerkin (PSPG) stabilizations is used to solve both the flow and adjoint equations. The airfoil is parametrized via a Non-Uniform Rational B-Splines (NURBS) curve. Three different objective functions are used to obtain optimal shapes: maximize lift, minimize drag and minimize ratio of drag to lift. The objective functions are formulated on the basis of time-averaged aerodynamic coefficients. The three objective functions result in diverse airfoil geometries. The resulting airfoils are thin, with the largest thickness to chord ratio being only 5.4%. The shapes obtained are further investigated for their aerodynamic performance. Maximization of time-averaged lift leads to an airfoil that produces more than six times more lift compared to the NACA 0012 airfoil. The excess lift is a consequence of the large peak and extended region of high suction on the upper surface and high pressure on the lower surface. Minimization of drag results in an airfoil with a sharp leading edge. The flow remains attached for close to 70% of the chord length. Minimization of the ratio of drag to lift results in an airfoil with a shallow dimple on the upper surface. It leads to a fairly large value of the time-averaged ratio of lift to drag (~17.8). The high value is mostly achieved by a 447% increase in lift and 16% reduction in drag, compared to a NACA 0012 airfoil. Imposition of volume constraint, for the cases studied, is found to result in airfoils that have lower aerodynamic performance.

1. Introduction

Airfoils operating at low Reynolds number ($Re < 5 \times 10^5$) are gaining increasing significance due to their utilization in a variety of applications such as micro-aerial vehicles (MAV), unmanned aerial vehicles (UAV), small wind turbines and high altitude remotely piloted vehicles (RPV) [1–4]. With the recent advances in manufacturing technology, the size of MAVs has shrunk. Airfoils are expected to have low drag and high lift to drag ratio. Conventional airfoils designed for high Reynolds numbers have been found to have a non-optimal performance at low *Re*. At low *Re*, viscous effects are relatively large leading to large drag and low lift to drag ratios.

Carmichael [5] suggested a critical *Re* of 5×10^4 for the flow to reattach after separation. The *Re* is based on the characteristic length, defined as the distance from the points of separation and reattachment. Airfoils operating below this *Re* do not achieve reattachment after laminar separation. The laminar boundary layer lacks momentum to overcome the adverse pressure gradient and, therefore, separates. Beyond $Re = 5 \times 10^4$, the laminar boundary layer, on separation, rapidly undergoes transition to a turbulent state. This flow may then reattach as a turbulent boundary layer leading to a region of enclosed recirculation called the laminar separation bubble.

Sunada et al. [6] experimentally measured the aerodynamic characteristics of fifteen airfoils at $Re = 4 \times 10^3$. The airfoils included several from the NACA four digit series with zero camber, flat plates with different thickness to chord ratios, thin plates with varied camber and a corrugated airfoil. They observed that at lower *Re*, the airfoils with better aerodynamic characteristics have to be thinner than those at higher *Re* and should also have a sharp leading edge. A thin plate with 5% camber, with its maximum occurring near the mid-chord section, yields the best performance. Null and Shkarayev [7] studied the effect of camber on a S5010-TOP24C-REF thin plate airfoil for $5 \times 10^4 \leq Re \leq 1 \times 10^5$. An airfoil at $Re = 7.5 \times 10^4$ with 3% camber yields a $C_{l_{max}}$ of 1.4 at $\alpha = 35°$. The maximum lift drag ratio of 6.5 is obtained at $\alpha = 5°$. They observed that a 3% camber airfoil is an optimal choice because of its larger lift to drag ratio and milder pitching moment close to stall.

Schmitz [8], while choosing an airfoil for a model airplane, carried out a detailed comparison of the performance of a flat plate, a 6% cambered thin plate, *G*625, *N*60 and *N*60*R* airfoils for $4.2 \times 10^4 \leq Re \leq 4.2 \times 10^5$. He observed that for a good performance, the lower the Reynolds number, the thinner must the profile of the airfoil be and the sharper its leading edge. Amongst the shapes that were considered, the cambered plate has the best aerodynamic characteristics. Its thickness to chord ratio is 2.9% with the maximum camber occurring at 40% of the chord from the leading edge. The maximum lift coefficient of this airfoil is $C_{l_{max}} = 1.06$ at

Corresponding author. Tel.: +91 512 259 7906; fax: +91 512 259 7561.
E-mail addresses: srinath@iitk.ac.in (D.N. Srinath), smittal@iitk.ac.in (S. Mittal).

0045-7825/$ – see front matter © 2010 Elsevier B.V. All rights reserved.
doi:10.1016/j.cma.2010.02.016

$\alpha = 8°$. Compared to the $C_{l_{max}}$ produced by flat plate and the *G*625 airfoil, this number is higher by 100–150%. The lift to drag ratio for this value of $C_{l_{max}}$ is 26. It was observed that for $Re < 1\times10^5$ the 6% cambered thin plate has the best performance because of (1) favourable pressure gradient at the leading edge, (2) large camber on the lower surface and (3) relatively forward position of the point of the maximum camber. Pelletier and Mueller [9] also investigated the aerodynamic characteristics for flat plates of different thickness and thin plates of a different camber for $6\times10^4 \le Re \le 2\times10^5$. A 4% cambered plate is seen to deliver the best performance. They observed that the trailing edge geometry does not affect the performance of the airfoils that were considered. Also, hysteresis, which is usually observed with thick airfoils, is not observed in the case of thin airfoil geometries. Kunz [10] numerically compared several 2% thick NACA four digit series airfoils. The flow field was assumed to be steady. He found that at $Re = 1.2\times10^4$, positioning the point of the maximum camber around 70% of the chord, and increasing the maximum camber leads to an increase in lift. An airfoil with 4% camber and with its maximum occurring at 70% chord produces a lift to drag ratio of 15.7. Table 1 lists the key details of the studies that have been summarized above. The listings in the table are restricted to the efforts for $4\times10^3 \le Re \le 6\times10^4$. The table shows the maximum value of the lift to drag ratio, and the conditions therein, for the various studies.

The wings of small insects, operating at $Re < 10^4$ do not have smooth airfoil sections. Rather, they are seen to have surfaces with discontinuities or pleats. Vargas, Mittal and Dong [11] studied the flow over a dragonfly wing and compared its performance with that of a smooth airfoil. They observed that the performance of the pleated airfoil is marginally better than that of a smooth one. The formation of recirculation zones within the pleats leads to a negative shear drag. They suggested that pleated airfoils can be good contenders for use in MAVs.

Optimization methods have found increased use in the design of aerodynamic components. A function which is a measure of the aerodynamic performance is identified and minimized. The optimization methods can be broadly classified on the basis of the utilization of the gradient in finding the optimal search direction. Non-gradient based methods do not use gradient information but only the values of the objective function. Simplex [12], simulated annealing [13] and genetic algorithms [14] are a few such methods that have been used in the design of airfoils. Gradient based methods use both the objective function and the gradient information to obtain an optimum. Complex Taylor series expansion approach [15], automatic differentiation methods [16], direct differentiation methods [17] and adjoint based methods [18,19] are a few that can be used to compute the gradient. Of particular interest are adjoint based methods. In these methods the cost of computing the gradient is independent of the number of design parameters. Adjoint based methods have found applications in diverse areas such as aerospace [20–23], marine [24] and bio-medical engineering [25]. These methods attempt to seek a local optimum. The possibility of the local optimum being the global optimum depends on the choice of initial guess used in the optimization process.

Adjoint based methods have been widely used for design in the steady flow regime. Only recently have these methods been employed in optimization in unsteady flows. Okumura and Kawahara [26] applied the adjoint method to reduce the force on the circular cylinder in a $Re = 200$ flow. A streamlined shape was achieved as a consequence of the drag reduction. Mani and Mavriplis [27] used the adjoint method for shape optimization of a pitching airfoil in an inviscid flow. They used an Arbitrary Lagrangian–Eularian (ALE) formulation with deforming mesh. Convergence was achieved only when the number of design variables is kept small. This problem was attributed to the complexity of the design space and the inability of the optimizer to navigate through it. Nadarajah and Tatossian [28], while solving the equations in the frequency domain, minimized the drag of a helicopter rotor blade while maintaining a constant lift. Srinath and Mittal [29] studied the effect of the extent of time integration on the optimization process while optimizing airfoil shapes at $Re = 1000$. It was noticed that, when computed for insufficient times, the gradients are likely to be erroneous. Unusual shapes, having high aerodynamic performances, were obtained. Inclusion of a constraint on the volume is found to limit the range of optimal shapes that can be obtained. Much attention, in the past, has been focussed on the design of airfoils at a single operating point. While this approach leads to airfoils with a better performance, the behavior at off-design conditions is generally poor. One possible way to alleviate this problem is to include off-design conditions in the design process. Several methods have been proposed. A few examples are the weighted multi-point approach [30–32], the profile optimization approach [33] and the probabilistic approach [34].

The objective of the present work is to apply the adjoint method for the determination of optimal airfoils at $Re = 1\times10^4$ and $\alpha = 4°$. The associated flow is unsteady. Therefore, the objective functions are based on time-averaged aerodynamic coefficients. Three different objective functions are considered: maximize lift coefficient, minimize drag coefficient and minimize ratio of drag to lift. The shapes obtained from the optimization process are analyzed to understand the way they improve the aerodynamic performance in comparison to conventional geometries. A finite element method based on streamline-upwind Petrov/Galerkin (SUPG) and pressure-stabilized Petrov–Galerkin (PSPG) stabilization techniques [35] is employed to solve, both, the flow and adjoint equations. The geometry of the airfoil is modelled by a 4th NURBS curve [36] with 13 control points. The Limited memory-Broyden–Fletcher–Goldfarb–Shanno (L-BFGS) algorithm [37] is used to minimize the objective function.

2. Governing equations

Let $\Omega \subset R^{n_{sd}}$ and $(0, T)$ be the spatial and temporal domains, respectively, where n_{sd} is the number of space dimensions. Let Γ represent the boundary of Ω. The spatial and temporal coordinates are denoted by x and t. The Navier–Stokes equations governing incompressible flow are

$$\rho\left(\frac{\partial u}{\partial t} + u.\nabla u\right) - \nabla.\sigma = 0 \text{ on } \Omega \times (0,T) \tag{1}$$

$$\nabla.u = 0 \text{ on } \Omega \times (0,T) \tag{2}$$

Here ρ, u and σ are the density, velocity and stress tensor, respectively. For a Newtonian fluid the stress tensor is given as $\sigma =$

Table 1
Compilation of results of other authors who carried out analysis in the Re range of 4×10^3 to 6×10^4. AR denotes the ratio of the span to the chord of a wing.

Researcher	*Re*	$(C_l/C_d)_{max}$	α at $(C_l/C_d)_{max}$	C_l at $(C_l/C_d)_{max}$	Geometry	
					Airfoil	Planform
Sunada (1997)	4×10^3	8.6	5°	0.75	Circular arc airfoil with 5% camber	Rectangular planform with AR = 6.75
Null et al. (2005)	5×10^4	4.25	5°	0.2	3% cambered S5010-TOP24C-REF plate airfoil	Circular planform with squared off leading edge
Schmitz (1967)	4.2×10^4	26	8°	1.06	Curved plate with 3% camber	Rectangular planform with AR = 5
Pelletier et al. (2000)	6×10^4	17	12°	1.1	Plate with 4% camber	Rectangular with AR = 1.5
Kunz (2003)	1.2×10^4	15.7	6°	0.65	NACA 4702 airfoil	2D, numerical study

$-pI+\mu[\nabla u+(\nabla u)^T]$ where, p is the pressure and I is the identity tensor. The boundary conditions are either on the flow velocity or stress. Both, Dirichlet and Neumann type boundary conditions are considered in the following form:

$$u = g \text{ on} \Gamma_g \tag{3}$$

$$n.\sigma = h \text{ on} \Gamma_h \tag{4}$$

where, n is the unit normal vector on the boundary Γ. Here, Γ_g and Γ_h are the subsets of the boundary Γ. More details on the boundary conditions are given in Fig. 1. Γ_U, Γ_D and Γ_S represent the upstream, downstream and lateral boundaries, respectively. The surface of the body is represented by Γ_B.

The initial condition on the velocity is specified as:

$$u(x,0) = u_0 \text{ on} \Omega \tag{5}$$

where u_0 is divergence free.

The drag and lift force coefficients, (C_d, C_l), on the body are calculated using the following expression:

$$(C_d,C_l) = \frac{2}{\rho U^2 S}\int_{\Gamma_B} \sigma n d\Gamma \tag{6}$$

The time-averaged coefficients are calculated as follows:

$$\overline{C}_d = \frac{1}{T}\int_{t_0}^{t_0+T} C_d(t)dt \tag{7}$$

$$\overline{C}_l = \frac{1}{T}\int_{t_0}^{t_0+T} C_l(t)dt \tag{8}$$

The time-averaging begins at $t=t_0$ to leave out the transient effect of the initial condition on the fully developed unsteady flow.

3. The adjoint approach

3.1. The augmented objective function

Let Γ_B be the segment of the boundary whose shape is to be determined. Let $\beta=(\beta_1, \ldots, \beta_m)$ be the set of shape parameters that determine Γ_B. The optimization problem involves finding the shape parameters that minimize (or maximize) the objective function, $I_c(U,\beta)$.

The flow Eqs. (1) and (2) are treated as constraint conditions on the objective function. An augmented objective function is constructed to convert the constrained problem to an unconstrained one. The flow equations are augmented to the objective function by introducing a set of Lagrange multipliers or adjoint variables $\Psi=(\psi_u, \psi_p)$.

$$I = I_c - \int_0^T\int_\Omega \psi_p \nabla.u d\Omega dt + \int_0^T\int_\Omega \psi_u.\left(\rho\left(\frac{\partial u}{\partial t} + u.\nabla u\right) - \nabla.\sigma\right)d\Omega dt \tag{9}$$

The augmented objective function (Eq. (9)) degenerates to the original one if the flow variables, $U=(u,p)$, exactly satisfy Eqs. (1) and (2). The variables ψ_u and ψ_p are referred to as the adjoint velocity and adjoint pressure, respectively. The first variation of the augmented objective function is given by:

$$\delta I = \frac{\partial I}{\partial U}\delta U + \frac{\partial I}{\partial \beta}\delta\beta + \frac{\partial I}{\partial \Psi}\delta\Psi \tag{10}$$

The optimal solution is achieved when the variation of the augmented objective function vanishes, i.e., $\delta I=0$. This requires that the variation of I with respect to the flow variables U, design parameters β and the adjoint variables Ψ should go to zero, independently. Variation of I with respect to U is given by:

$$\frac{\partial I}{\partial U} = \frac{\partial I_c}{\partial U} - \frac{\partial}{\partial U}\int_0^T\int_\Omega \psi_p \nabla.u d\Omega dt + \frac{\partial}{\partial U}\int_0^T\int_\Omega \psi_u.\left(\rho\left(\frac{\partial u}{\partial t} + u.\nabla u\right) - \nabla.\sigma\right)d\Omega dt \tag{11}$$

The above relation, when set to zero, leads to a set of equations and boundary conditions that are used to evaluate the adjoint variables. This will be described in more detail in the following sub-section. Variation of I with respect to Ψ gives back the flow Eqs. (1) and (2). The gradient, $\frac{\partial I}{\partial \beta}$, is utilized to find the optimal shape parameters. It quantifies the sensitivity of the objective function to the design parameters. It is used by the optimizer to refine the search direction. The vanishing of the gradient reflects the attainment of optimal shape. The gradient is evaluated using the following expression:

$$\frac{\partial I}{\partial \beta} = \frac{\partial I_c}{\partial \beta} - \frac{\partial}{\partial \beta}\int_0^T\int_\Omega \psi_p \nabla.u d\Omega dt + \frac{\partial}{\partial \beta}\int_0^T\int_\Omega \psi_u.\left(\rho\left(\frac{\partial u}{\partial t} + u.\nabla u\right) - \nabla.\sigma\right)d\Omega dt \tag{12}$$

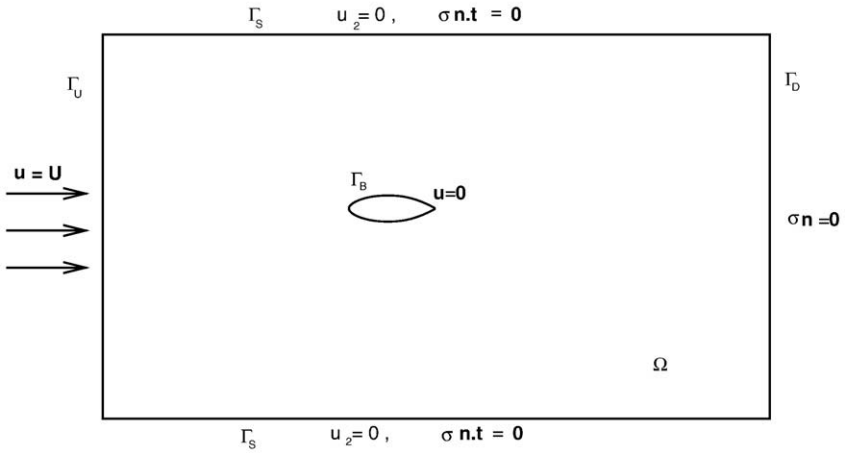

Fig. 1. Schematic of the problem set-up: boundary conditions. Γ_U, Γ_D and Γ_S are the upstream, downstream and lateral boundaries, respectively and Γ_B is the body surface.

3.2. The adjoint equations and related boundary and terminal conditions

The equations and boundary conditions for the adjoint variables are obtained by setting the variation of I with respect to the flow variables U, given in Eq. (11), to zero. The equations governing the adjoint variables are:

$$\rho\left(-\frac{\partial \psi_u}{\partial t} + (\nabla u)^T \psi_u - (u.\nabla)\psi_u\right) - \nabla.\sigma_\psi = 0 \text{ on } \Omega \times (0,T) \tag{13}$$

$$\nabla.\psi_u = 0 \text{ on } \Omega \times (0,T) \tag{14}$$

where, σ_ψ is similar to the stress tensor and is given by $\sigma_\psi = -\psi_p I + \mu[\nabla\psi_u + (\nabla\psi_u)^T]$.

The boundary conditions on the adjoint variables are:

$$\psi_u = 0 \text{ on } \Gamma_U \tag{15}$$

$$s = 0 \text{ on } \Gamma_D \tag{16}$$

$$s_1 = 0,\ \psi_{u2} = 0 \text{ on } \Gamma_S \tag{17}$$

$$-\int_0^T \int_{\Gamma_B} \delta\left(\sigma.n\right).\psi_u d\Gamma dt + \frac{\partial I_c}{\partial u}\delta u + \frac{\partial I_c}{\partial p}\delta p = 0 \text{ on } \Gamma_B \tag{18}$$

where, $s = \{u\psi_u - I\psi_p + \nu[\nabla\psi_u + (\nabla\psi_u)^T]\}.n$. The terminal condition on the adjoint velocity is given by:

$$\psi_u(u,T) = 0 \text{ on } \Omega \tag{19}$$

The adjoint Eqs. (13) and (14) are a set of coupled linear partial differential equations. Unlike the flow Eqs. (1) and (2), the equations for the adjoint variables are posed backward in time. In the present work, the adjoint variables are computed once the time integration of the flow equations has been carried out. All the results are stored for use in evaluating the gradient.

4. Finite element formulation

4.1. Flow equations

The domain Ω is discretized into elements Ω^e, $e = 1,2,\ldots,n_{el}$, where n_{el} is the number of elements. Let S_u^h and S_p^h be the appropriate finite element spaces and $\mathcal{V}_u^h$ and $\mathcal{V}_p^h$ the weighing function spaces for velocity and pressure, respectively. The stabilized finite element formulation of Eqs. (1) and (2) is written as follows: find $u^h \in S_u^h$ and $p^h \in S_p^h$ such that $\forall w^h \in \mathcal{V}_u^h$, $q^h \in \mathcal{V}_p^h$,

$$\begin{aligned}
&\int_\Omega w^h.\rho\left(\frac{\partial u^h}{\partial t} + u^h.\nabla u^h\right)d\Omega + \int_\Omega \in\left(w^h : \sigma\left(p^h,u^h\right)\right)d\Omega \\
&\quad + \int_\Omega q^h \nabla.u^h d\Omega + \sum_{e=1}^{n_{el}} \int_{\Omega^e} \frac{1}{\rho}\left(\tau_{SUPG}\rho u^h.\nabla w^h + \tau_{PSPG}\nabla q^h\right). \\
&\quad \left[\rho\left(\frac{\partial u^h}{\partial t} + u.\nabla u\right) - \nabla.\sigma\right]d\Omega^e \\
&\quad + \sum_{e=1}^{n_{el}} \int_{\Omega^e} \tau_{LSIC}\nabla.w^h \rho \nabla.u^h d\Omega^e = \int_{\Gamma^h} w^h.h^h d\Gamma.
\end{aligned} \tag{20}$$

The first three terms and the right-hand side in the variational formulation given by Eq. (20) constitute the Galerkin formulation of the problem. The terms involving the element level integrals are the stabilization terms added to the basic Galerkin formulation to enhance its numerical stability. These terms stabilize the computations against node-to-node oscillations in advection dominated flows and allow the use of equal-in-order basis functions for velocity and pressure. The terms with coefficients τ_{SUPG} and τ_{PSPG} are based on the SUPG (streamline-upwind/Petrov–Galerkin) and PSPG (pressure-stabilized/Petrov–Galerkin) stabilizations. For the definition of these coefficients the interested reader is referred to the article by Tezduyar et al. [35]. The term with coefficient τ_{LSIC} is a stabilization term based on the least squares of the incompressibility constraint. Equal-in-order basis functions for velocity and pressure are used. A three point quadrature is employed for numerical integration. Marching in time is done via the generalized trapezoidal rule (Crank–Nicholson method).

4.2. Adjoint equations

A stabilized SUPG/PSPG finite element method is proposed to solve the adjoint Eqs. (13) and (14). Let $S_{\psi u}^h$ and $S_{\psi p}^h$ be the appropriate finite element spaces and $\mathcal{V}_{\psi u}^h$ and $\mathcal{V}_{\psi p}^h$ the corresponding weighting function spaces for the adjoint velocity and adjoint pressure. The stabilized finite element formulation of Eqs. (13) and (14) is written as follows: given u^h and p^h satisfying Eqs. (1) and (2), find ψ_u^h $S_{\psi u}^h$ and ψ_p^h $S_{\psi p}^h$ such that $\forall w_{\psi u}^h$ $\mathcal{V}_{\psi u}^h$, $q_{\psi p}^h$ $\mathcal{V}_{\psi p}^h$,

$$\begin{aligned}
&\int_\Omega w_{\psi_u}^h.\rho\left(-\frac{\partial \psi_u^h}{\partial t} + \left(\nabla u^h\right)^T \psi_u^h - u.\nabla\psi_u\right)d\Omega \\
&\quad + \int_\Omega \in\left(w_{\psi_u}^h\right) : \sigma_\psi\left(\psi_p^h,\psi_u^h\right)d\Omega + \int_\Omega q_{\psi_p}^h \nabla.\psi_u^h d\Omega \\
&\quad + \sum_{e=1}^{n_{el}} \int_{\Omega^e} \frac{1}{\rho}\left(\tau_{SUPG}\left(\rho\left(\nabla u^h\right)^T w_{\psi_u}^h - \rho u^h.\nabla w_{\psi_u}^h\right) + \tau_{PSPG}\nabla q_{\psi_p}^h\right). \\
&\quad \left[\rho\left(-\frac{\partial \psi_u^h}{\partial t} + \left(\nabla u^h\right)^T \psi_u^h - u.\nabla\psi_u\right) - \nabla.\sigma_\psi\left(\psi_p^h,\psi_u^h\right)\right]d\Omega^e \\
&\quad + \sum_{e=1}^{n_{el}} \int_{\Omega^e} \tau_{LSIC}\nabla.w_{\psi_u}^h \rho \nabla.\psi_u^h d\Omega^e = 0
\end{aligned} \tag{21}$$

The stabilization coefficients τ_{SUPG}, τ_{PSPG} and τ_{LSIC} in the formulation proposed in Eq. (21) are computed based on the flow variables (u, p). For solving the adjoint equations, the flow solution is required at every time step. In the present work the flow solution is written to disk after every time step. After the time integration of flow equations has been carried out the adjoint solver reads the flow solution from the disk. The time spent in the input/output operations is found to be negligible compared to the overall solution time. This approach is expected to be very demanding on storage when extended to three-dimensions. It is also possible to use proper orthogonal decomposition (POD) to reduce storage. The POD may be used to construct a basis for the unsteady flow. The storage of the basis is expected to be significantly cheaper than the storage of the entire unsteady flow data. Such an approach has been used in the context of

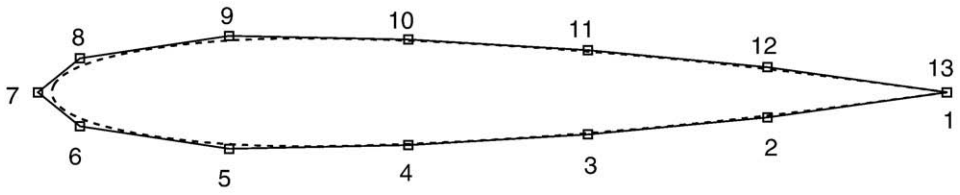

Fig. 2. Representation of NACA 0012 airfoil with a NURBS curve with 13 control points. Points 1, 7 and 13 are held fixed while the y-coordinates of the remaining ten control points are used as design variables. The broken line shows the resulting curve.

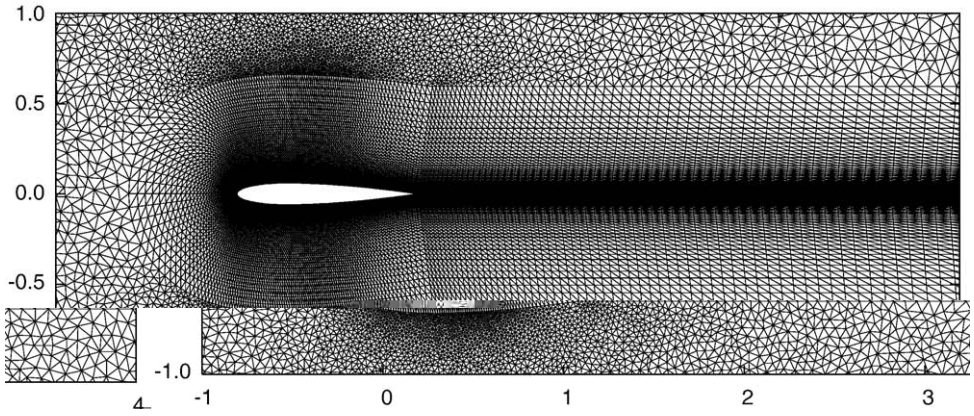

Fig. 3. Close up view of the finite element mesh for the NACA 0012 airfoil at 0° angle of attack. The mesh consists of 46,730 nodes and 93,156 triangular elements with 200 nodes on the airfoil surface.

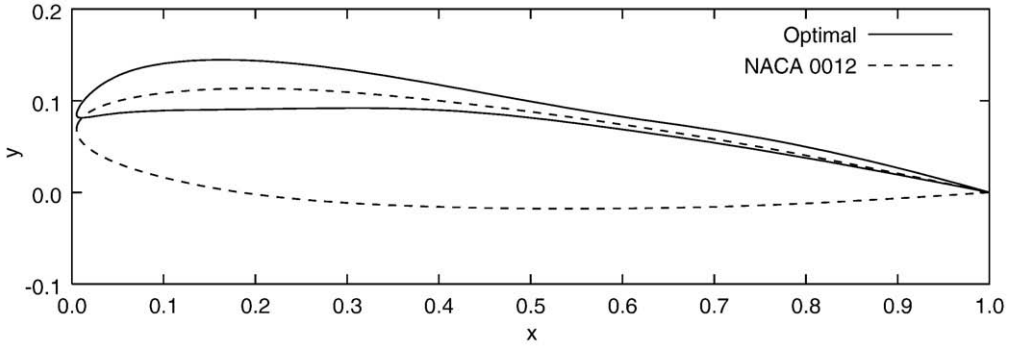

Fig. 4. Maximization of $\bar{C}_l$ at $Re = 1 \times 10^4$ and $\alpha = 4°$: optimal and initial shapes.

optimal control of vortex shedding [38,39] and control of flow separation over a forward facing step [40].

5. Parametrization

A 4th order NURBS (Non-Uniform Rational Bi-cubic Spline) curve is utilized to parametrize the airfoil surface. Based on the recommendations of Lepine et al. [41] only 13 control points are used. Fig. 2 shows the representation of a NACA 0012 airfoil at 0° angle of attack obtained from a NURBS parametrization. The corresponding control polygon along with the control points is also shown. The first and the last control points overlap to ensure a closed geometry. The control points at the leading edge and trailing edge are held fixed to preserve the chord length and angle of attack. The y-coordinates of the remaining ten control points are used as the design parameters.

6. The optimizer

The optimization algorithm used in the present work is the L-BFGS (Limited memory-Broyden–Fletcher–Goldfarb–Shanno) procedure

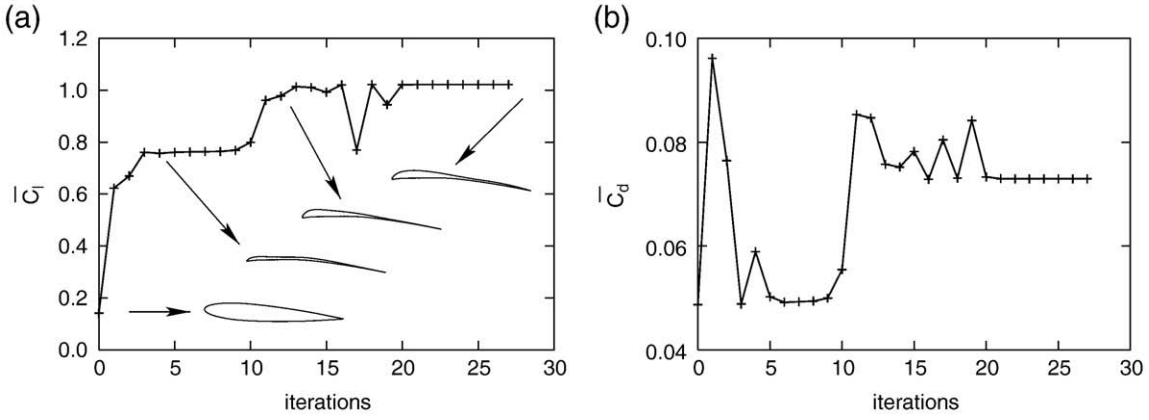

Fig. 5. Maximization of $\bar{C}_l$ at $Re = 1 \times 10^4$ and $\alpha = 4°$: iteration history of (a) $\bar{C}_l$ and (b) $\bar{C}_d$. A few intermediate shapes obtained during the optimization process are also shown.

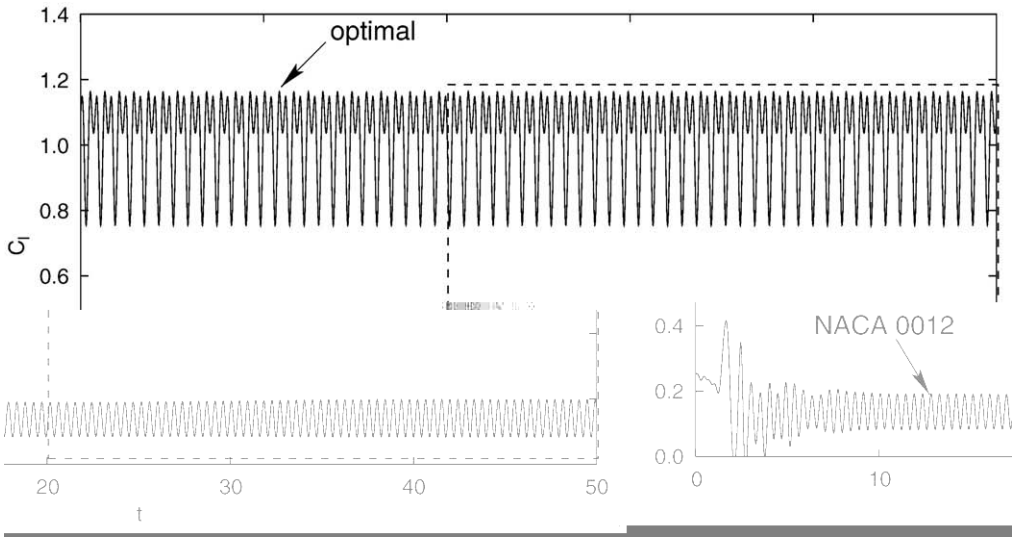

Fig. 6. Maximization of time-averaged lift coefficient at $Re = 1 \times 10^4$, $\alpha = 4°$: time history of lift coefficient of optimal and NACA 0012 airfoils. The control window is also shown.

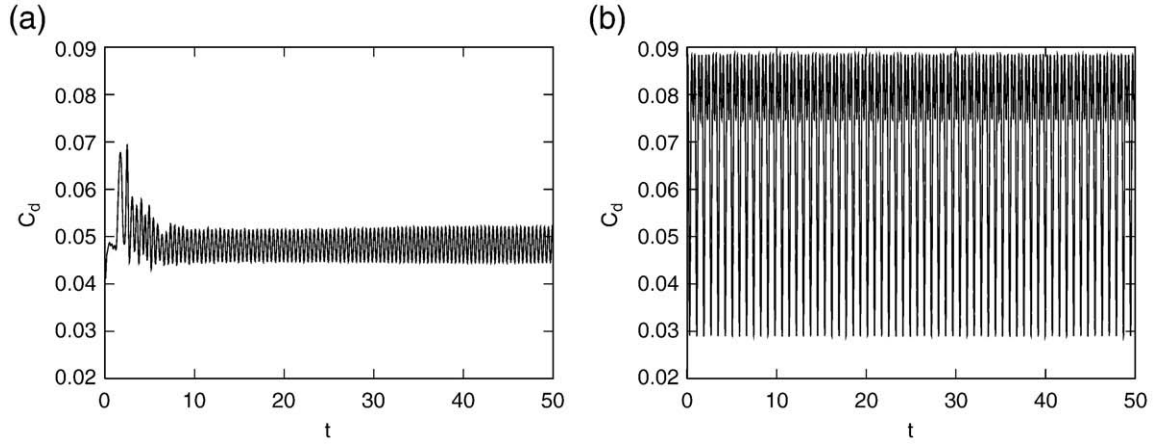

Fig. 7. Maximization of time-averaged lift coefficient at $Re = 1 \times 10^4$, $\alpha = 4°$: time history of drag coefficient of (a) NACA 0012 and (b) optimal airfoils.

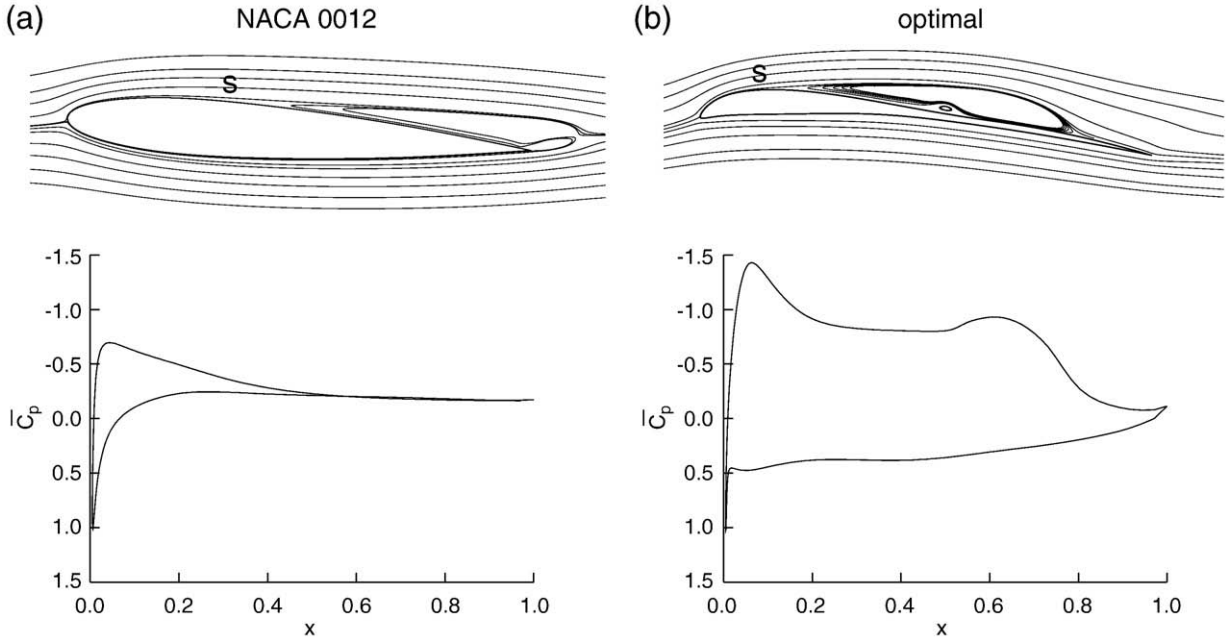

Fig. 8. Airfoil design for maximum time-averaged lift coefficient at $Re = 1 \times 10^4$, $\alpha = 4°$: time-averaged streamlines over NACA 0012 and optimal airfoils. The location of the point of flow separation, 's', is also shown.

[37]. This is a limited memory quasi-Newton method for solving large nonlinear optimization problems that are constrained by upper and lower bounds on the design variables. The algorithm is well suited for problems when the information for the second derivative (the Hessian) is difficult to obtain.

7. Implementation of the optimization procedure

A brief description of the sequence of steps in implementing the optimization procedure is presented. An objective function, I_c, which quantifies the desired properties is identified. The surface which is to be optimized is then parametrized by a suitable set of design parameters, β. An initial shape is assumed and a finite element mesh is generated for this shape. Next, the flow variables u and p are computed via Eq. (20). Using the flow variables, the adjoint variables ψ_u and ψ_p are determined by solving Eq. (21). The entire data for the flow and the adjoint variables are stored on disk. Next, the gradient is evaluated using Eq. (12). The objective function and the gradient information are passed to the optimization algorithm to obtain an update on the design parameters. The finite element mesh is modified to accommodate the new shape. A mesh moving scheme is used to achieve this. The entire procedure is repeated till a convergence criterion, either on the gradient or objective function, is satisfied.

8. Results

Optimization is carried out to determine an airfoil shape with the best aerodynamic performance. The Reynolds number, based on the chord of the airfoil, is 1×10^4 for all the computations. The angle of attack is 4°. The flow is unsteady in this situation. Therefore, the

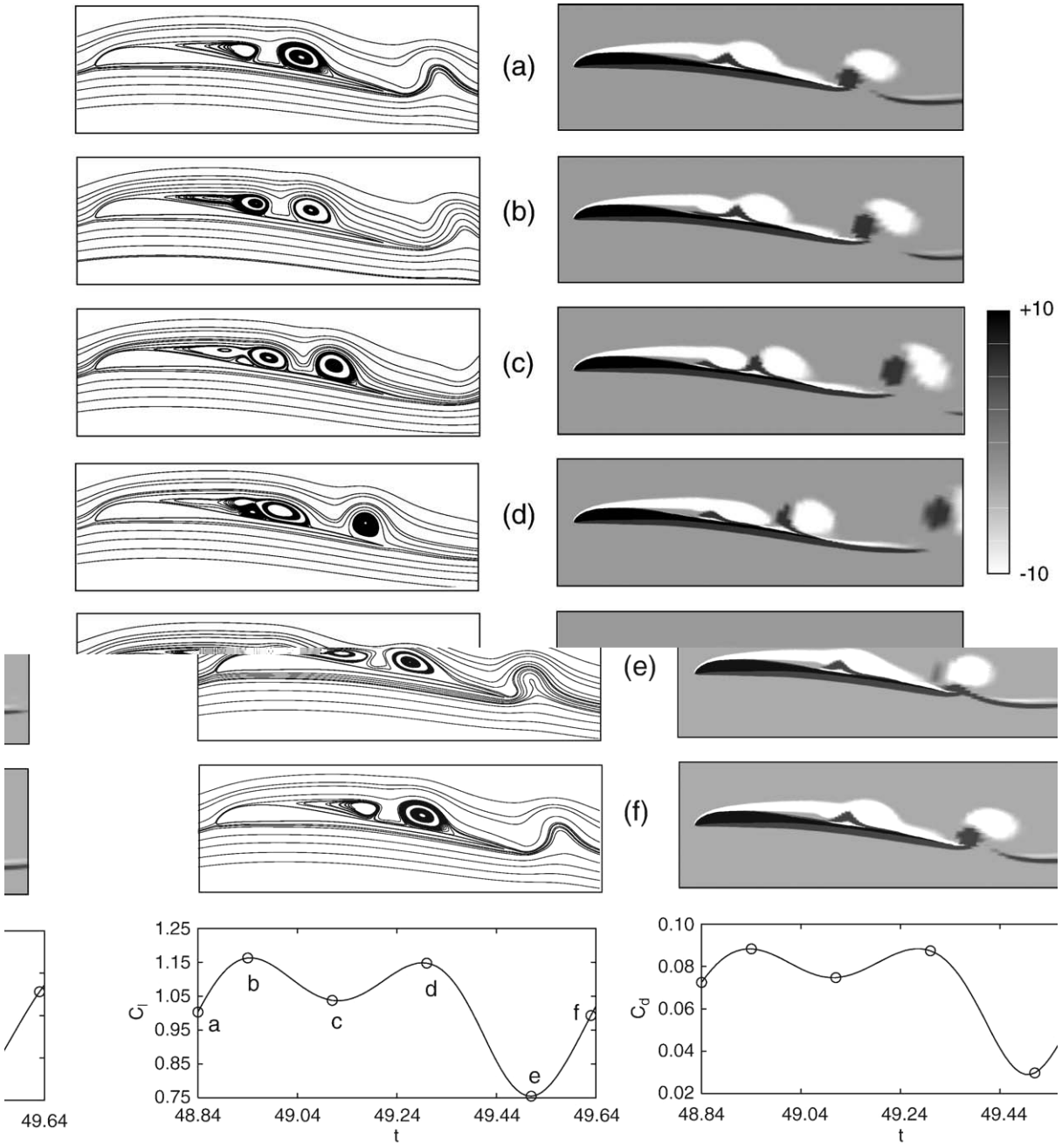

Fig. 9. Airfoil design for maximum time-averaged lift coefficient at $Re=1\times10^4$, $\alpha=4°$: stream function and vorticity field for the optimal shape at various time instants during one cycle of time variation of C_l. The time instants at which the flow is shown are marked on the time histories of the lift and drag coefficients in the bottom row.

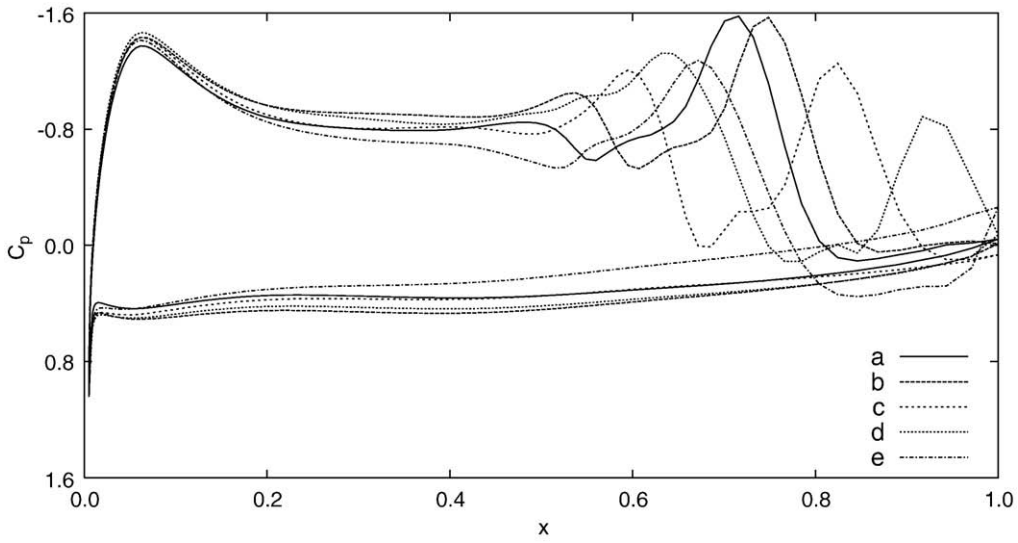

Fig. 10. Airfoil design for maximum time-averaged lift coefficient at $Re = 1 \times 10^4$, $\alpha = 4°$: C_p distribution at various time instants of the shedding cycle for the optimal shape.

objective function is based on time-averaged aerodynamic coefficients. Three objective functions are chosen: (a) maximization of $\overline{C}_l$, (b) minimization of $\overline{C}_d$ and (c) minimization of $\overline{C}_d / \overline{C}_l$. For all the computations in the present work, NACA 0012 airfoil is used as the initial guess. A close up view of the finite element mesh used for the computation is shown in Fig. 3. The mesh consists of 46,730 nodes and 93,156 triangular elements with 200 nodes on the airfoil surface. A structured mesh is employed near the airfoil surface and in the near wake to resolve the flow structures adequately. The remaining domain is filled with an unstructured mesh obtained via Delaunay triangulation. A mesh moving scheme [42] is utilized to relocate the nodes of the mesh to accommodate the modified airfoil geometry.

8.1. Maximization of time-averaged lift

The objective is to determine an airfoil shape that has the largest time-averaged lift coefficient. The objective function is given by $I_c = -\frac{1}{2}\overline{C}_l^2$. The shape obtained at the end of the optimization cycle is shown along with the initial shape in Fig. 4. The optimal shape has a thickness to chord ratio of 5.4%. The iteration history of $\overline{C}_l$ and $\overline{C}_d$ is shown in Fig. 5. The optimal airfoil has a time-averaged lift coefficient of 1.02 as compared to 0.14 for the NACA 0012 airfoil. 28 design iterations are required for the optimizer to converge. Also shown are a few intermediate shapes obtained during the design cycle. The time histories of C_l for the optimal and NACA 0012 airfoil are shown in Fig. 6. Flow over the optimal airfoil is associated with larger unsteadiness as can be seen from the larger magnitude of oscillation of the lift coefficient. The control window for which the adjoint and gradients are computed is also shown. It extends for 30 time units. For an accurate computation of the gradients, the control window should extend over several shedding cycles. More details regarding choosing the extent of the control window can be found in the work by Srinath and Mittal [29]. The optimal shape is associated with, approximately, 50% more time-averaged drag as compared to the NACA 0012 airfoil. This is not surprising since the objective function is based solely on the lift coefficient and is, therefore, unaffected by the drag. The time histories of the drag coefficient for the NACA 0012 and optimal airfoils are shown in Fig. 7.

The C_p distribution of the time-averaged flow of both the optimal and NACA 0012 airfoil is shown in Fig. 8. The value of the peak suction on the upper surface of the optimal airfoil is much larger than that on the NACA 0012 airfoil. The pressure on the lower surface is also higher for the optimal airfoil. This leads to the increased time-averaged lift generated by the optimal airfoil. The figure also shows the time-averaged streamlines for the NACA 0012 and the optimal airfoils. Flow past the NACA 0012 airfoil separates at, approximately, 40% of the chord. It separates at 20% of the chord for the optimal airfoil. The stream function and the vorticity fields for the optimal shape at various time instants during one cycle of time variation of C_l are shown in Fig. 9. The frequency of vortex shedding is smaller than that for the NACA 0012 airfoil. The C_p distribution on the optimal airfoil at time instants corresponding to those shown in Fig. 9 is shown in Fig. 10. The time evolution of the vortices on the upper surface of the optimal airfoil can be clearly seen in Fig. 9. Vortices, whose cores are at located at $x \sim 0.5c$, are shed periodically. This is seen in Fig. 9 as well as from the suction peaks in Fig. 10. The first peak in the suction occurs near the leading edge of the airfoil. The later peaks are related to the presence of vortex structures. The vortex, after it is shed, becomes stronger and moves downstream. The increase in strength can also be noticed from the increase in peak suction at the core of the vortex. It starts becoming weaker once it reaches $x \sim 0.75c$ and leaves the airfoil as shown in the last frame of Fig. 9 and from the C_p distribution shown

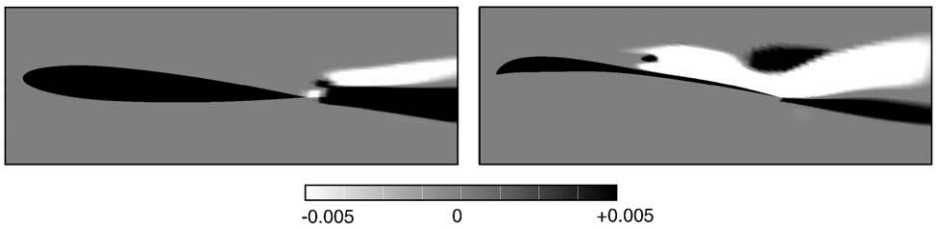

Fig. 11. Airfoil design for maximum time-averaged lift coefficient at $Re = 1 \times 10^4$, $\alpha = 4°$: $\overline{u\,v}$ component of correlations of the perturbations with respect to the mean flow for NACA 0012 (left) and optimal airfoil (right).

in Fig. 10. While the vortex convects, a new one forms on the airfoil at $x \sim 0.5c$. Therefore, at almost all time instants, there are two vortices on the surface of the airfoil. During the period, such as at '*e*', when there is only one vortex, on the surface of the airfoil, there is only one local peak in the suction on the airfoil surface. This leads to lower than the time-averaged lift experienced by the airfoil. As compared to the NACA 0012 airfoil, the flow over the optimal airfoil is associated with large unsteadiness. The $\overline{u\,v}$ component of the correlations of the velocity fluctuations, with respect to the mean flow, is shown in Fig. 11. Large magnitude of $\overline{u\,v}$ on the upper surface confirms the increased unsteadiness in the flow over the optimal airfoil. It is this vortical activity that is responsible for the higher time-averaged suction on the airfoil surface and, consequently, larger lift.

8.1.1. Maximization of time-averaged lift with volume constraint

We now investigate the effect of imposing a volume constraint on the aerodynamic performance of the optimal airfoil. An inverse constraint on the volume of the airfoil is included in the objective function; the modified objective function is given as: $I_c = -\frac{1}{2}\overline{C}_l^2 + \gamma\frac{1}{2}(V-V_0)^2$. The weight, γ, is appropriately chosen to ensure that both the terms in the objective function contribute, approximately, equally. If γ is too small, the term related to the volume might get overwhelmed by the term

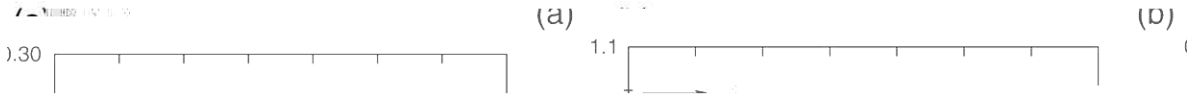

Fig. 12. Airfoil design for maximum time-averaged lift coefficient with volume constraint at $Re = 1 \times 10^4$, $\alpha = 4°$: (a) iteration history of $\overline{C}_l$, (b) volume enclosed, (c) time history of C_l, (d) C_d and (e) optimal and initial shapes. Optimal-1 refers to the shape obtained using the shape obtained from lift maximization without volume constraint as the initial guess, while Optimal-2 refers to that from the NACA 0012 airfoil.

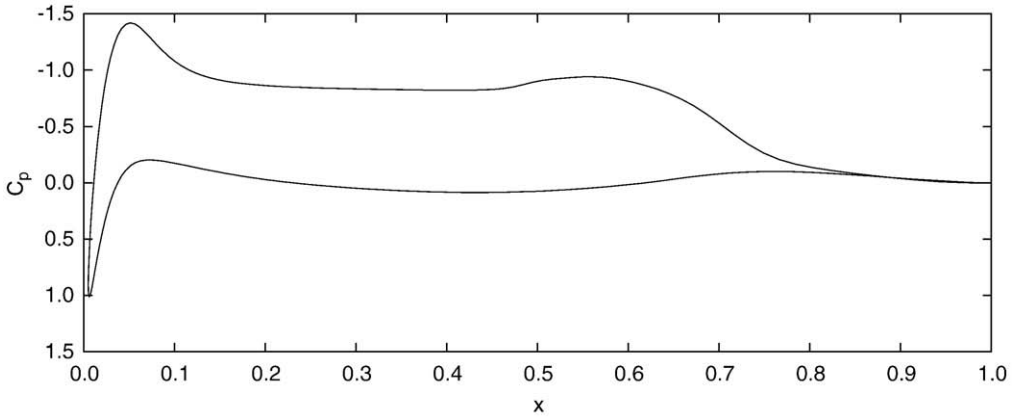

Fig. 13. Airfoil design for maximum time-averaged lift coefficient with volume constraint at $Re = 1 \times 10^4$, $\alpha = 4°$: $\overline{C_p}$ distribution.

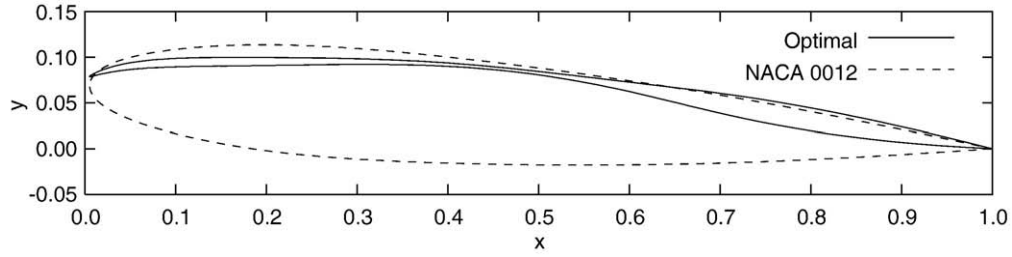

Fig. 14. Minimization of $\overline{C_d}$ at $Re = 1 \times 10^4$ and $\alpha = 4°$: optimal and initial shapes.

involving $\overline{C_l}$. On the other hand, if it is too large, the volume constraint might get satisfied well but only at the expense of aerodynamic performance. This has been addressed in earlier articles in the context of steady [43] and unsteady flows [29]. In this work, results are presented for $\gamma = 1000$ and $V_0 = 0.1$. The NACA 0012 airfoil, of the unit chord, has a volume of 0.08. We recall that the present optimization method finds local optima. Two sets of computations have been carried out. In the first, the NACA 0012 airfoil is used as the initial guess. These computations result in an airfoil with rather low $\overline{C_l}$ ($= 0.435$, as opposed to 1.02 for an airfoil without volume constraint). In the second set of computations, the optimal shape obtained from the lift maximization without volume constraint is used as the initial guess. The volume of the airfoil used for the initial guess is 0.025. The iteration histories of $\overline{C_l}$ and the enclosed volume are shown in Fig. 12(a) and (b). The optimal airfoil, from this approach, leads to a time-averaged lift coefficient of 0.65. Although this value of $\overline{C_l}$ is higher than the one with NACA 0012 as an initial guess, a 35% reduction in the aerodynamic performance is observed as an outcome of imposing the volume constraint. The error in satisfaction of the volume is less than 1%. A few intermediate shapes obtained during the optimization process are shown in Fig. 12(a). The time histories of the lift and drag coefficients for the optimal shape are shown in Fig. 12(c) and (d). The optimal shapes obtained from the two sets of computations are shown in Fig. 12(e). The airfoil with, volume constraint, is associated with a bulbous leading edge and bulges/bumps on the upper and lower surfaces at, approximately, 80%

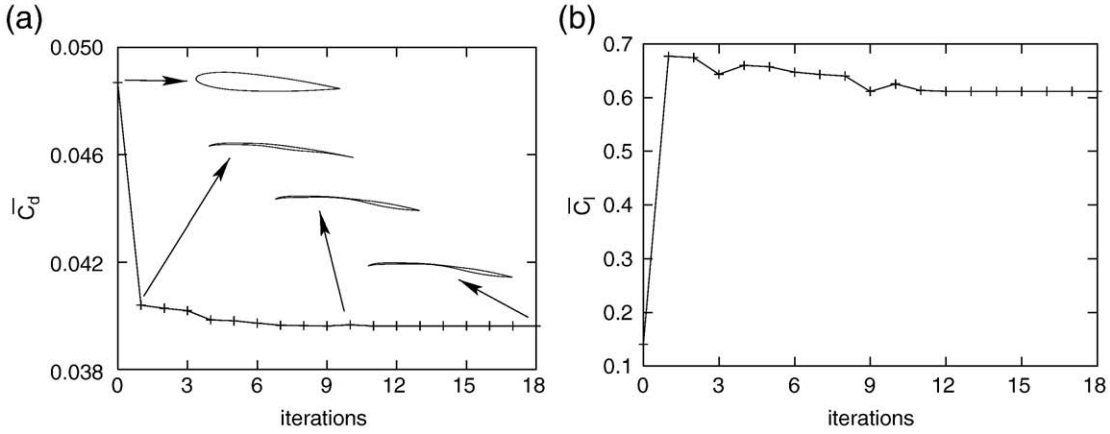

Fig. 15. Minimization of $\overline{C_d}$ at $Re = 1 \times 10^4$ and $\alpha = 4°$: iteration history of (a) $\overline{C_d}$ and (b) $\overline{C_l}$. A few intermediate shapes obtained during the optimization process are also shown.

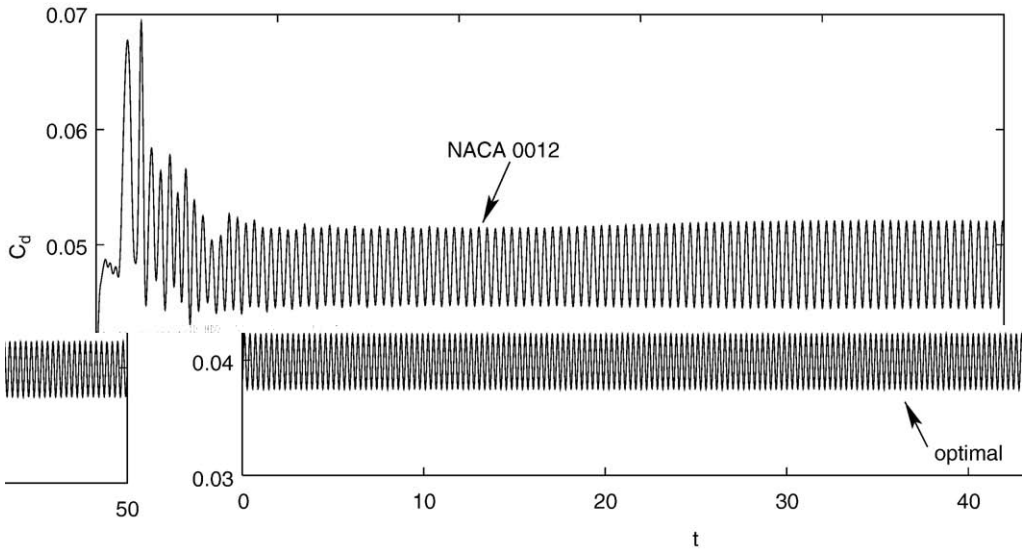

Fig. 16. Minimization of $\overline{C_d}$ at $Re = 1 \times 10^4$ and $\alpha = 4°$: time history of C_d for the NACA 0012 and optimal airfoils.

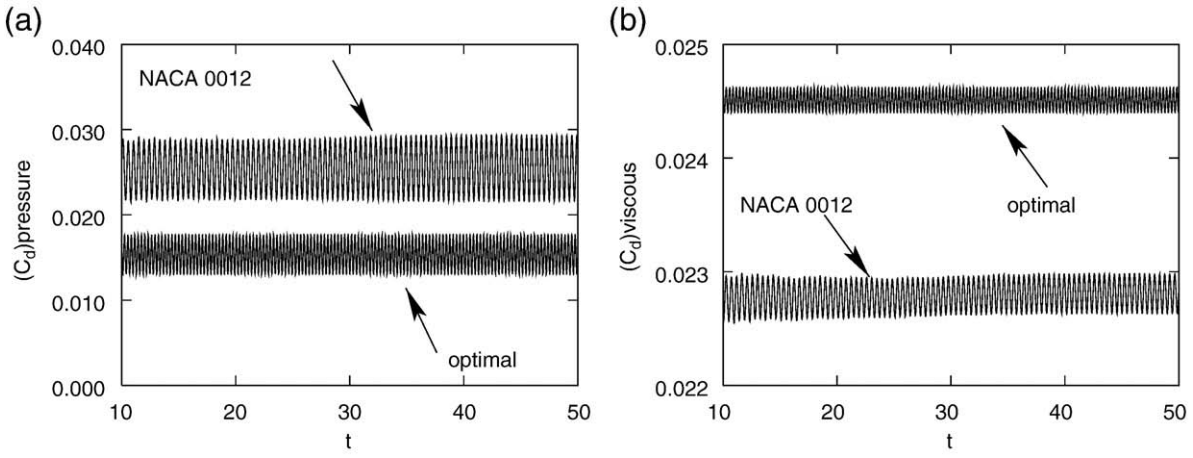

Fig. 17. Minimization of $\overline{C_d}$ at $Re = 1 \times 10^4$ and $\alpha = 4°$: time histories of the pressure and viscous components of the drag coefficient for the NACA 0012 and optimal airfoils.

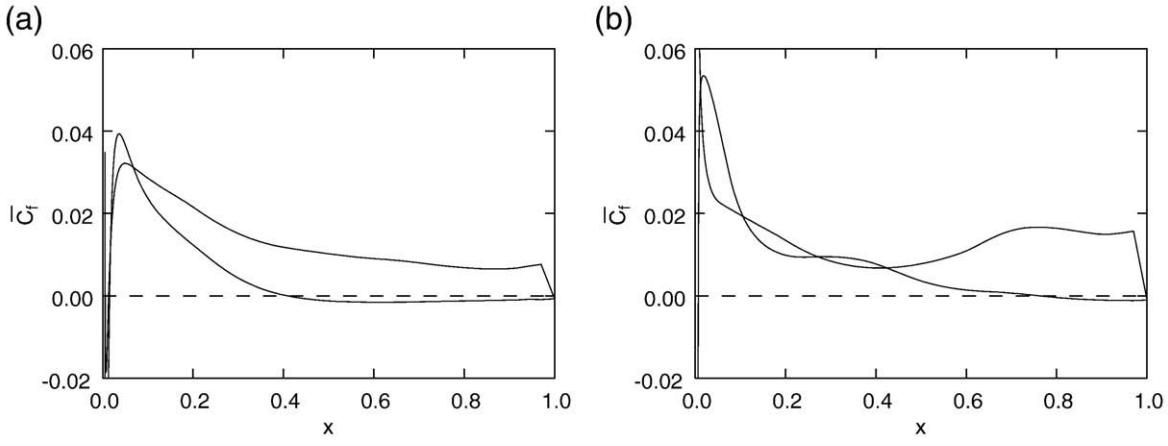

Fig. 18. Minimization of $\overline{C_d}$ at $Re = 1 \times 10^4$ and $\alpha = 4°$: time-averaged skin friction coefficient over (a) NACA 0012 and (b) optimal airfoil.

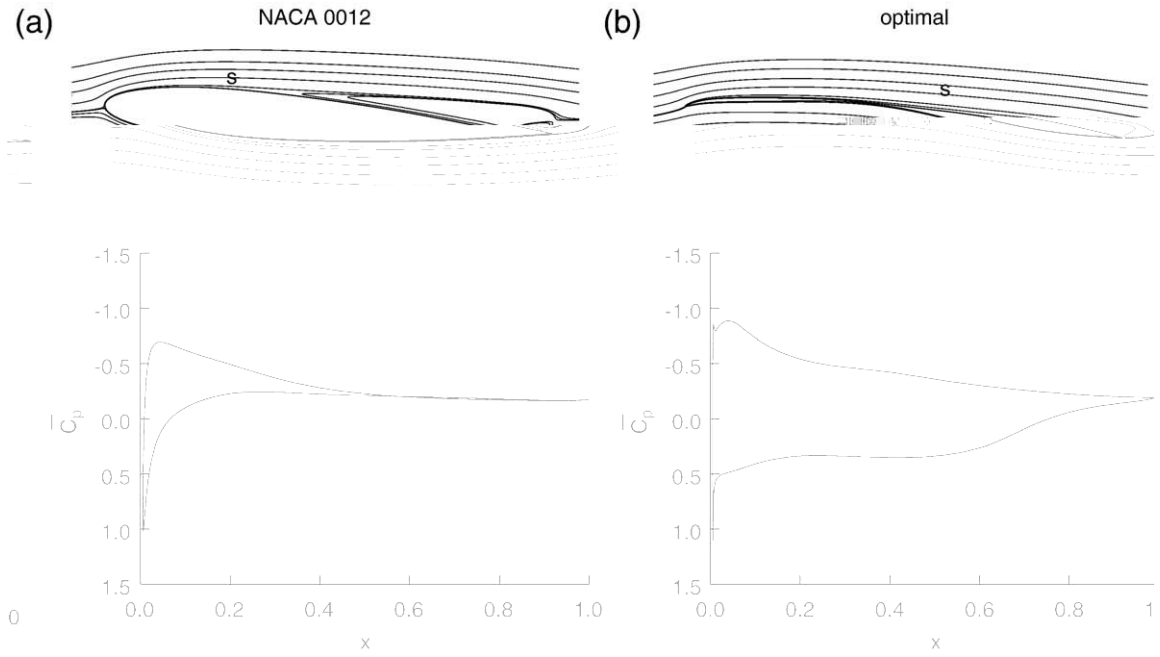

Fig. 19. Minimization of $\overline{C_d}$ at $Re = 1 \times 10^4$ and $\alpha = 4°$: time-averaged streamlines and C_p distribution for the NACA 0012 and the optimal airfoils. *s* denotes the location of the point of flow separation.

of the chord from the leading edge. It has larger thickness than the one without the constraint. As a result, the drag is also larger. Interestingly, the pressure component of the drag is comparable for both the initial and optimal airfoils. However, the skin friction component is smaller for the optimal airfoil without volume constraint. The time-averaged C_p distribution of the optimal airfoil is shown in Fig. 13. Comparing the $\overline{C_p}$ distribution of the initial shape, shown in Fig. 8(b), with that in Fig. 13 it is noticed that both the airfoils have a large suction peak near the leading edge. However, the airfoil with no volume constraint is associated with larger pressure on the lower surface. This accounts for the higher lift generation.

8.2. Minimization of time-averaged drag

The objective is to determine an airfoil shape with the least time-averaged drag. The objective function is given by $I_c = \frac{1}{2}\overline{C}_d^2$. The optimal airfoil is seen to be a thin body with a bulge on the lower surface towards the trailing edge. This is shown in Fig. 14 along with the NACA 0012 airfoil. This shape has a time-averaged drag coefficient of 0.0396, which corresponds to an 18% reduction from that of the NACA 0012 airfoil. The iteration histories of $\overline{C_d}$ and $\overline{C_l}$ are shown in Fig. 15 along with a few intermediate shapes obtained during the design process. A drag coefficient, close to the optimal value, is achieved right after one iteration. The corresponding shape is thin and has a small bulge on the lower surface near the mid-chord section. In the next few iterations, the bulge moves towards the trailing edge. Very few changes in the shape take place beyond ten iterations. The time histories of C_d of both the NACA 0012 and the optimal airfoil are shown in Fig. 16. The amplitude of oscillation of drag for the optimal airfoil is smaller compared to that of the NACA 0012 airfoil. However, the frequency of vortex shedding is higher.

To investigate the cause of reduction in drag, we examine the contribution from pressure and viscous components. The time histories of the pressure and viscous parts of the drag are shown in Fig. 17. Compared to the NACA 0012 airfoil, the optimal airfoil shows a 40% reduction in pressure drag. However, the viscous drag increases by 8%. To further examine the cause for the increase in the viscous contribution, the distribution of the local surface skin friction for the time-averaged flow is computed and shown in Fig. 18. Compared to the NACA 0012 airfoil, the optimal airfoil has large shear stresses near the leading edge. This is probably due to the sharp leading edge of the optimal airfoil. Larger shear stresses are also observed in the bulge region near the trailing edge on the lower surface. Time-averaged streamlines for both the NACA 0012 and the optimal airfoils are shown in Fig. 19. The very significant drop in the pressure drag of the optimal airfoil is due to the delay in the separation of the flow. The separation point for the time-averaged flow for the optimal airfoil is $0.77c$, approximately, which is significantly aft of that for the NACA 0012 airfoil ($\simeq 0.4c$). The time-averaged pressure coefficient is shown in the bottom row of Fig. 19. The optimal airfoil generates almost four times more lift than the NACA 0012 airfoil. A region of reasonably high suction occurs on the

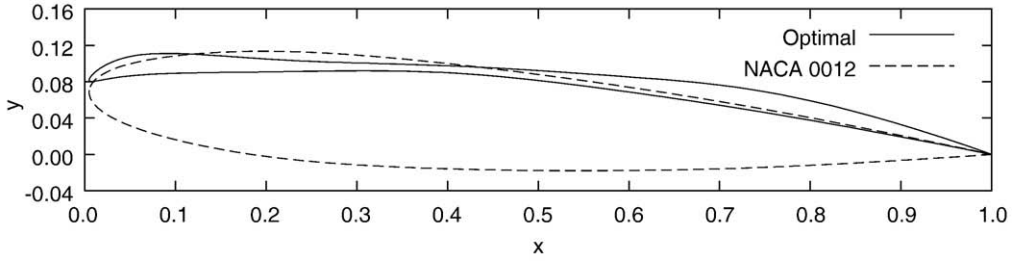

Fig. 20. Minimization of time-averaged drag to lift ratio at $Re = 1 \times 10^4$, $\alpha = 4°$: optimal and initial shapes.

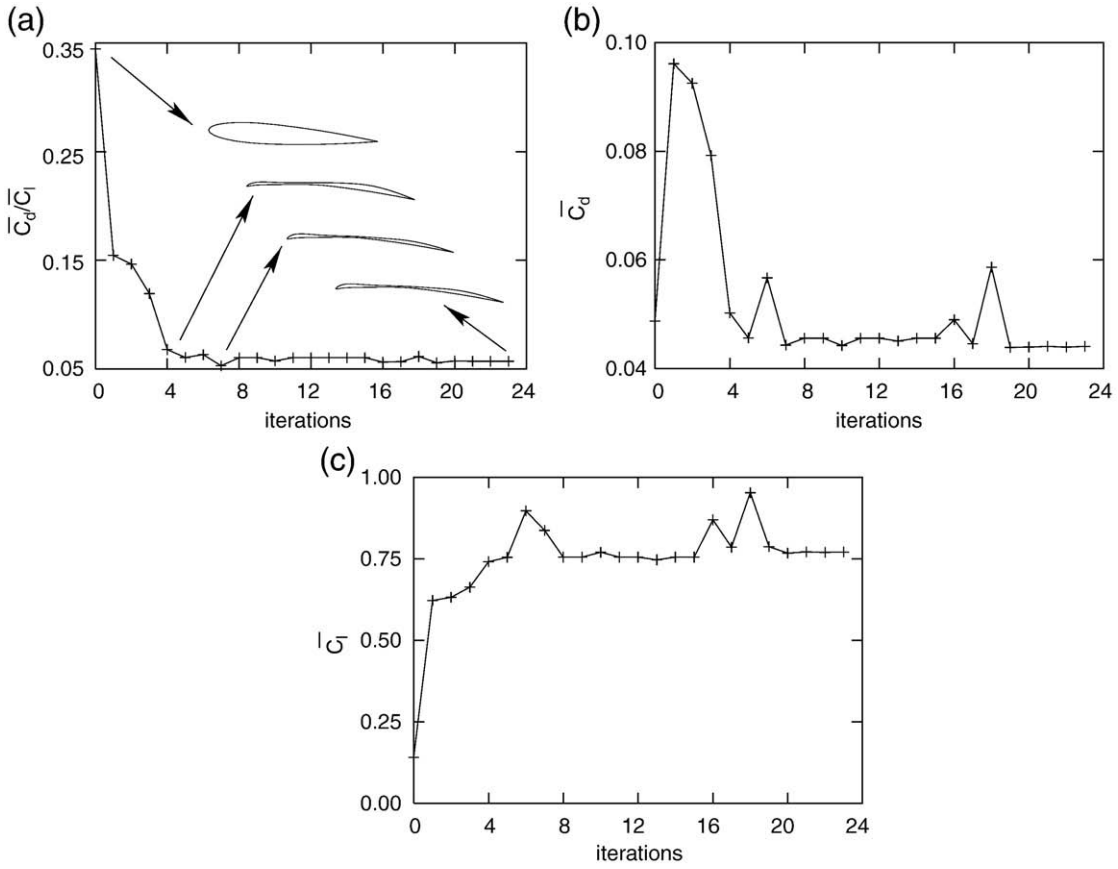

Fig. 21. Minimization of time-averaged drag to lift ratio at $Re = 1 \times 10^4$, $\alpha = 4°$: iteration history of (a) $\overline{C_d} / \overline{C_l}$, (b) $\overline{C_d}$ and (c) $\overline{C_l}$.

upper surface while a region of high pressure exists on the lower surface. This leads to a significantly larger $\overline{C_l}$ for the optimal airfoil, compared to the NACA 0012 geometry.

8.3. Minimization of ratio of time-averaged drag to lift

The objective function in this case is defined as: $I_c = \frac{1}{2}\left(\frac{\overline{C_d}}{\overline{C_l}}\right)^2$. The optimal shape obtained at the end of the design cycle is shown in Fig. 20 along with the NACA 0012 airfoil. The optimal shape has a small bulbous leading edge and a small bulge on the upper surface near the trailing edge. The thickness to chord ratio of the optimal airfoil is 3%. A relatively long and shallow dimple is observed on the upper surface of the optimal airfoil. The time-averaged drag to lift ratio for the optimal shape is 0.057 as compared to 0.345 of the NACA 0012 airfoil. This corresponds to an 83.5% reduction in value. In terms of lift to drag ratio, the optimal airfoil represents a five-fold increase in the performance. A similar dimple was observed by the authors

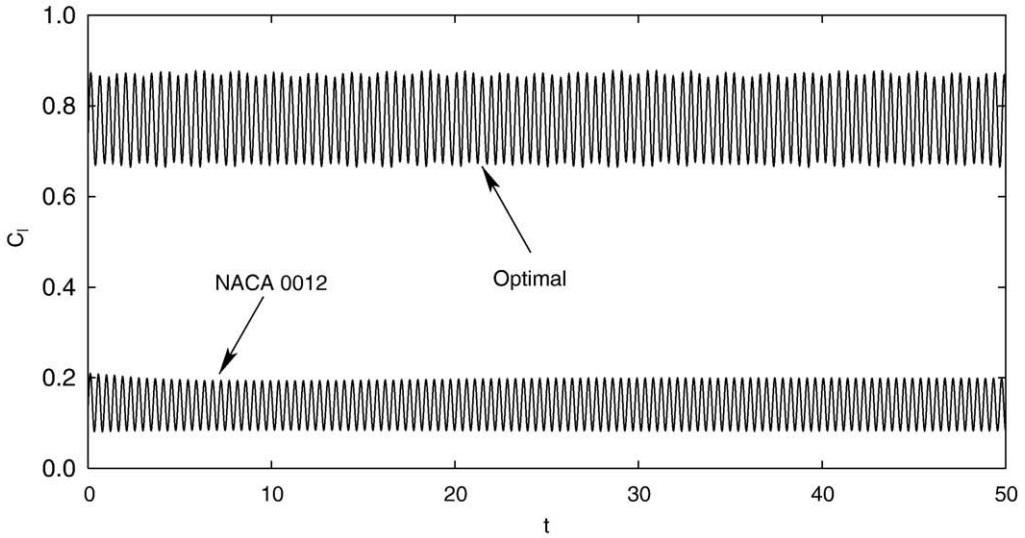

Fig. 22. Minimization of time-averaged drag to lift ratio at $Re = 1 \times 10^4$, $\alpha = 4°$: time history of C_l for optimal and NACA 0012 airfoils.

[43] while optimizing an airfoil shape in steady flows at $Re = 250$. Eliminating the dimple by straightening the surface led to lower values of lift and higher values of drag.

The time-averaged drag decreases only by 16% while the lift increases by 445% for the optimal airfoil. The iteration history of the time-averaged drag to lift ratio is shown in Fig. 21 along with a few intermediate shapes. The iteration histories of $\overline{C}_d$ and $\overline{C}_l$ are also shown in the figure. The time history of C_l for, both, initial and optimal airfoils is shown in Fig. 22. Flow over the optimal airfoil exhibits a slight increase in the amplitude of oscillation. The frequency of vortex shedding is also marginally lower than that of the NACA 0012 airfoil. Fig. 23 shows the pressure and viscous contribution to C_d for the NACA 0012 and the optimal airfoils. For the optimal airfoil, the contributions of pressure and viscous stress to C_d decrease by 8% and 14%, respectively, compared to the NACA 0012 airfoil. The C_p distribution of the time-averaged flows over both the optimal and initial airfoils is shown in Fig. 24. While the peak suction on the upper surface is larger than that of the NACA 0012 airfoil, it is lesser than that of the optimal shape obtained for maximum time-averaged lift. The lower surface also exhibits higher pressure resulting in a net increase in the time-averaged lift. Fig. 24 also shows the time-averaged streamlines over the NACA 0012 and optimal airfoils. For the optimal airfoil, the flow separates very close to the leading edge and reattaches near the mid-chord section leading to a very thin region of trapped flow. It separates again close to the trailing edge. The separation and reattachment points of the flow are marked in the figure.

8.4. Comparison of the optimal shapes

The aerodynamic and geometric characteristics of the optimal airfoils obtained for a different objective are shown in Table 2. The optimal shapes are also shown in the last column of this table. The results obtained are consistent with the objectives. However, the nature of flow varies for the different optimal shapes. The airfoil with the largest $\overline{C}_l$ has a bulbous leading edge, thickness to chord ratio of 5.4% and a maximum camber of 5.5%. The maximum camber is located fairly fore at $0.32c$. A large suction peak near the leading edge on the upper surface, a region of constant pressure on the upper surface owing to an early flow separation and a high pressure region on the lower surface due to increased camber combine to give a large increase in the time-averaged lift coefficient. The optimal airfoil, for minimal drag, is very thin with a sharp leading edge. The maximum thickness to chord ratio is 2.4%. The low thickness to chord ratio of the airfoil helps in reducing the pressure drag considerably by a significant delay in the flow separation. The separation point for this airfoil is located at $0.77c$. The airfoil with the least $\overline{C}_d / \overline{C}_l$ has a small bulbous leading edge. Its thickness to chord ratio is 2.2%. The strong suction peak leads to an increased lift. A shallow dimple on the upper surface of the airfoil leads to a small region of recirculation. The final separation point is located at $\sim 0.8c$. The increase in the lift to drag ratio is mostly due to the increased lift; the reduction in drag, compared to the NACA 0012 airfoil is 16%. Maximum camber for this airfoil occurs near the mid-chord section.

9. Conclusions

A continuous adjoint method is utilized for the design of airfoils in unsteady viscous flows for $\alpha = 4°$ and $Re = 1 \times 10^4$. A stabilized finite element method based on the SUPG/PSPG stabilizations has been used to solve, both, flow and adjoint equations. The airfoil surface is parametrized by a 4th order NURBS curve with 13 control points. The y-coordinates of the control points are used as the design parameters.

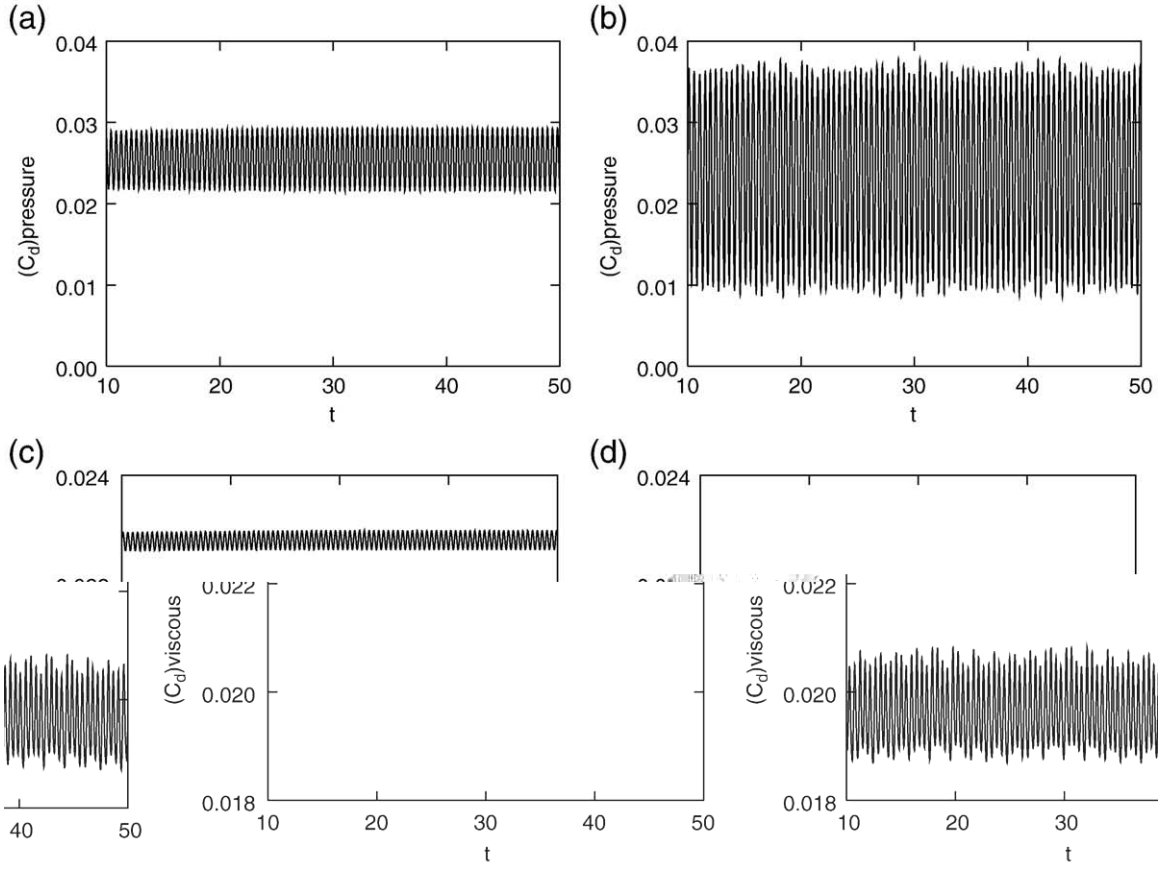

Fig. 23. Minimization of time-averaged drag to lift ratio at $Re = 1 \times 10^4$, $\alpha = 4°$: time histories of the pressure and viscous components of drag for the NACA 0012 and optimal airfoils. Figures (a) and (c) are for the NACA 0012 airfoil while (b) and (d) are for the optimal airfoil.

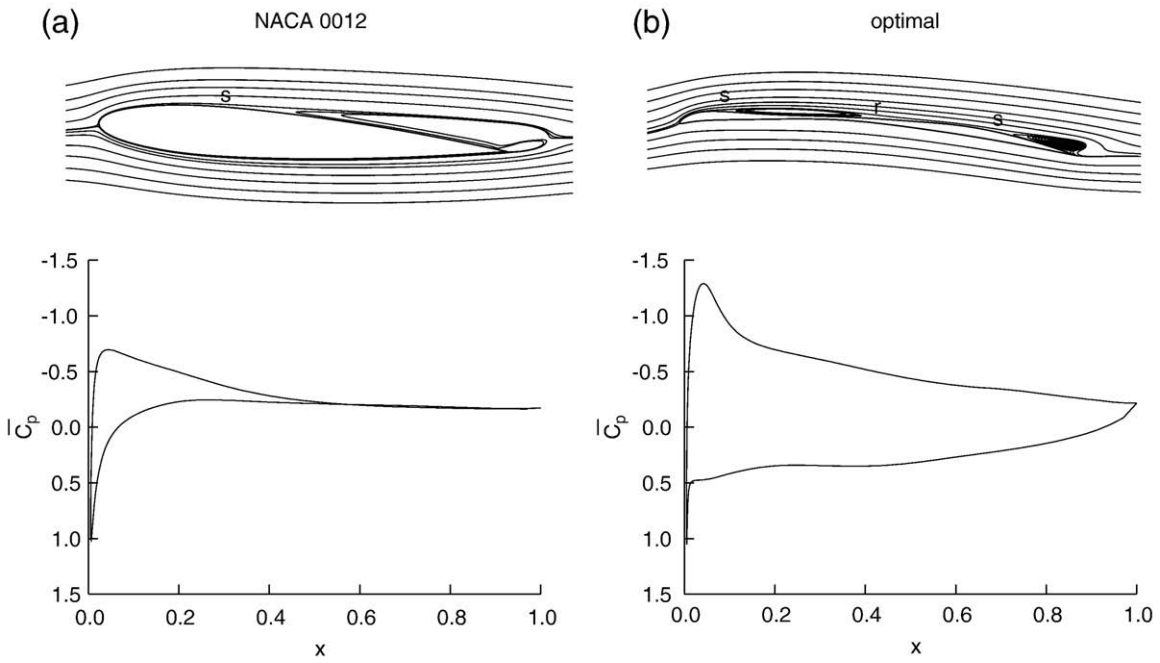

Fig. 24. Minimization of time-averaged drag to lift ratio at $Re = 1 \times 10^4$, $\alpha = 4°$: time-averaged stream lines and $\overline{C}_p$ distribution over the optimal and NACA 0012 airfoils. *s* and *r* denote the location of points of flow separation and reattachment, respectively.

Table 2
Comparison of the optimal shapes obtained for various objective functions at $Re = 1 \times 10^4$ and $\alpha = 4^o$. $\bar{x}_s$ is the location of the point of flow separation on the upper surface with respect to the leading edge, $-\overline{C}_{p_{\max}}$ is the maximum suction on the upper surface, $(t/c)_{\max}$ is the maximum thickness to chord ratio and x_{camber} is the location of the point of the maximum camber with respect to the leading edge.

I_c	$\overline{C}_l$	$\overline{C}_d$	$\overline{C}_l / \overline{C}_d$	$\bar{x}_s/c$	$-\overline{C}_{p_{\max}}$	$(t/c)_{\max}$	Max camber	x_{camber}	Final shape
Max $\overline{C}_l$	1.022	0.0729	14.00	0.20	1.43	5.4%	5.5%	0.32*c*	
Min $\overline{C}_d$	0.612	0.0396	15.45	0.77	0.88	2.4%	4.4%	0.42*c*	
Min $\overline{C}_d / \overline{C}_l$	0.771	0.0441	17.48	0.12	1.29	2.3%	4.7%	0.47*c*	
NACA 0012	0.141	0.0487	2.89	0.40	0.70	12.00%	0.0%	–	

The NACA 0012 airfoil is the initial guess for the computations. The L-BFGS algorithm is used as the optimizer.

Airfoils are designed for three different objective functions: maximize time-averaged lift coefficient, minimize time-averaged drag coefficient and minimize ratio of time-averaged drag to lift. Fairly diverse geometries are obtained while using various objective functions. The optimal airfoils are thin with the largest thickness to chord ratio being only 5.5%. The optimal airfoil obtained while maximizing the time-averaged lift has a lift coefficient more than five times that of the NACA 0012 airfoil. A strong suction peak, mild adverse pressure gradient for a considerable length on the upper surface and a large high pressure region on the lower surface are seen to be the cause for the large increase in lift. The flow remains attached for 70% of the length of the optimal airfoil obtained while minimizing the time-averaged drag coefficient. The reduction in drag is, approximately, 18% from that of the NACA 0012 airfoil. The optimal airfoil obtained from minimizing the ratio of time-averaged drag to lift ratio has a small bulbous leading edge and a shallow dimple on the upper surface. The recirculation zone present in the dimple reduces the viscous drag while the bulbous leading edge leads to a region of strong suction on the upper surface. The decrease in the time-averaged drag to lift ratio is 83.5%. The effect of the imposition of volume constraint is explored via modification of the objective function. For the cases studied, the volume constraint leads to airfoils that have a lower aerodynamic performance. This study demonstrates the ability of the method to obtain high performance airfoils in unsteady flows.

References

[1] T.J. Mueller, J.C. Kellogg, P.G. Ifju, S. Shkarayev, Introduction to the design of fixed — wing micro air vehicles, AIAA Education Series, 2006.
[2] T.J. Mueller, J.D. DeLaurier, Aerodynamics of small vehicles, Annu. Rev. Fluid Mech. 35 (2003) 89–111.
[3] P.B.S. Lissaman, Low-Reynolds number airfoils, Annu. Rev. Fluid Mech. 15 (1983) 223–239.
[4] G.R. Spedding, P.B.S. Lissaman, Technical aspects of microscale flight systems, J. Avian Biol. 29 (1998) 458–468.
[5] B.H. Carmichael, Low Reynolds Number Airfoil Survey, Volume 1, 1981, NASA-CR-165803-vol-1.
[6] S. Sunada, A. Sakaguchi, K. Kawachi, Airfoil section characteristics at low Reynolds numbers, J. Fluids Engrg. 119 (1997) 129–135.
[7] W. Null, S. Shkarayev, Effects of camber on the aerodynamics of adaptive-wing micro air vehicles, J. Aircr. 42 (2005) 1537–1542.
[8] F.W. Schmitz, Aerodynamics of the Model Airplane. Part I: Airfoil Measurements, 1967, NACA TM X-60976.
[9] A. Pelletier, T.J. Mueller, Low Reynolds number aerodynamics of low-aspect-ratio, thin/flat/cambered-plate wings, J. Aircr. 37 (2000) 825–832.
[10] P.J. Kunz. Aerodynamics and design for ultra-low Reynolds number flight. PhD dissertation, Stanford University, 2003.
[11] A. Vargas, R. Mittal, H. Dong, A computational study of the aerodynamic performance of a dragonfly wing section in gliding flight, Bioinspir. Biomim. 3 (2008) 26004.
[12] D. Landman, C.P. Britcher, Experimental geometry optimization techniques for multi-element airfoils, J. Aircr. 37 (2000) 707–713.
[13] X. Wang, M. Damodaran, S.L. Lee, Inverse transonic airfoil design using parallel simulated annealing and computational fluid dynamics, AIAA J. 40 (2002) 791–794.
[14] S. Obyashi, Aerodynamic inverse optimization with genetic algorithms, J. Engrg. Appl. Sci. (1996) 421–425.

[15] C.O.E. Burg, J.C. Newman III, Computationally efficient, numerically exact design derivatives via the complex Taylor series expansion method, Comput. Fluids 32 (2003) 373–383.
[16] L.L. Sherman, V.C. Taylor III, L.L. Green, P.A. Newman, G.J.W. Hou, M. Korivi, First and second order aerodynamic sensitivity derivatives via automatic differentiation with incremental iterative methods, J. Comput. Phys. 129 (1994) 307–331.
[17] G.J.W. Hou, J.S. Sheen, C.H. Chuang, Shape sensitivity analysis and design optimization of linear thermoelastic solids, AIAA J. 30 (1992) 528–537.
[18] B. Mohammadi, O. Pirroneau, Shape optimization in fluid mechanics, Annu. Rev. Fluid Mech. 36 (2004) 255–279.
[19] M.B. Giles, N.A. Pierce, An introduction to the adjoint approach to design, Flow Turbul. Combust. 65 (2000) 393–415.
[20] B. Mohammadi, Optimization of aerodynamic and acoustic performances of supersonic civil transports, Int. J. Numer. Methods Fluids 14 (2004) 891–907.
[21] J. Reuthers, A. Jameson, J. Farmer, L. Martinelli, D. Saunders, Aerodynamic shape optimization of complex aircraft configurations via adjoint formulations, AIAA Paper, 96-0094, 1996.
[22] S. Kim, J.J. Alonso, A. Jameson, Two-dimensional high lift aerodynamic optimization using the continuous adjoint method, AIAA Paper, 2000–4741, 2000.
[23] O. Soucy, S.K. Nadarajah, C. Balloch, Sonic boom reduction via remote inverse adjoint approach, AIAA Paper, 07–0056, 2007.
[24] O. Soto, R. Lohner, C. Yang, An adjoint-based design methodology for CFD problems, Int. J. Numer. Methods Heat Fluid Flow 14 (2004) 734–759.
[25] F. Abraham, M. Behr, M. Heinkenschloss, Shape optimization in steady blood flow: a numerical study of non-Newtonian effects, Comput. Methods Biomech. Biomed. Engrg. 8 (2005) 127–137.
[26] H. Okumura, M. Kawahara, Shape optimization of a body located in incompressible Navier–Stokes flow based on optimal control theory, Comput. Model. Engrg. Sci. 1 (2000) 71–77.
[27] K. Mani, D.J. Mavriplis, Unsteady discrete adjoint formulation for two-dimensional flow problems with deforming meshes, AIAA J. 46 (2008) 1351–1364.
[28] S.K. Nadarajah, C. Tatossian, Multi-objective aerodynamic shape optimization for unsteady viscous flows, Optim. Engrg. 11 (2010) 67–106.
[29] D.N. Srinath, S. Mittal, An adjoint method for shape optimization in unsteady viscous flows, J. Comput. Phys. 229 (2010) 1994–2008.
[30] M. Nemec, D.W. Zingg, T.H. Pulliam, Multipoint and multi-objective aerodynamic shape optimization, AIAA J. 42 (2004) 1057–1065.
[31] D.W. Zingg, S. Elias, Aerodynamic shape optimization under a range of operating conditions, AIAA J. 44 (2006) 2787–2792.
[32] D.N. Srinath, S. Mittal, Veera Manek, Multi-point shape optimization of airfoils at low Reynolds numbers, Comput. Model. Engrg. 51 (2009) 169–189.
[33] W. Li, L. Huyse, S. Padula, Robust airfoil optimization to achieve drag reduction over a range of Mach numbers, Struct. Multi. Optim. 24 (2002) 38–50.
[34] L. Huyse, S. Padula, R.M. Lewsi, W. Li, Probablistic approach to free-form airfoil shape optimization under uncertainity, AIAA J. 40 (2002) 1764–1772.
[35] T.E. Tezduyar, S. Mittal, S.E. Ray, R. Shih, Incompressible flow computations with stabilized bilinear and linear equal order interpolation velocity pressure elements, Comput. Meth. Appl. Mech. Engrg. 95 (1992) 221–242.
[36] Gerald Farin, Curves and Surfaces for Computer Aided Geometric Design. A Practical Guide, Academic Press, 1990.
[37] R.H. Byrd, P. Lu, J. Nocedal, C. Zhu, A limited memory algorithm for bound constrained optimization, SIAM J. Sci. Comput. 16 (1995) 1190–1208.
[38] J. Peraire, W.R. Graham, K.Y. Tang, Optimal control of vortex shedding using low-order models. Part I — open-loop model development, Int. J. Numer. Methods Engrg. 44 (1999) 945–972.
[39] M. Bergmann, L. Cordier, Optimal control of the cylinder wake in the laminar regime by trust-region methods and pod reduced-order models, J. Comput. Phys. 227 (2008) 7813–7840.
[40] S.S. Ravindran, Control of flow separation over a forward-facing step by model reduction, Comput. Meth. Appl. Mech. Engrg. 191 (2002) 4599–4617.
[41] J. Trepanier, J. Lepine, F. Guibault, F. Pepin, Optimized nonuniform rational b-spline geometrical representation for aerodynamic design of wings, AIAA J. 39 (2001) 2033–2041.
[42] T.E. Tezduyar, M. Behr, S. Mittal, A.A. Johnson, Computation of unsteady incompressible flows with the finite element methods — space–time formulations, iterative strategies and massively parallel implementations, in: P. Smolinski, W.K. Liu, G. Hulbert, K. Tamma (Eds.), New Methods in Transient Analysis, AMD-Vol.143, ASME, New York, 1992, pp. 7–24.
[43] D.N. Srinath, S. Mittal, Optimal airfoil shapes for low Reynolds number flows, Int. J. Numer. Methods Fluids 61 (2009) 353–381.